Journal of Materials Chemistry A

ROYAL SOCIETY OF CHEMISTRY

PAPER

View Article Online
View Journal | View Issue

Cite this: J. Mater. Chem. A, 2022, 10, 18383

One-pot microwave synthesis of Pd modified titanium dioxide nanocrystals for 3D aerogel monoliths with efficient visible-light photocatalytic activity in a heated gas flow reactor†

Junggou Kwon,[a] Kyoungjun Choi,[b] Elena Tervoort[a] and Markus Niederberger *[a]

Harvesting solar energy and efficiently converting it into a chemical energy carrier like hydrogen (H_2) is an important topic in photocatalysis. Here, we present a fast and simple approach for the one-pot synthesis of crystalline semiconductor nanoparticles modified with co-catalysts that can be used as nanobuilding blocks for nanoparticle-based aerogels with excellent visible-light photocatalytic activity. The microwave-assisted nonaqueous sol–gel method allows titanium dioxide (TiO_2) nanoparticles to be synthesized and modified with palladium (Pd) ions and Pd metal nanoparticles in a single step. Their assembly into aerogel monoliths preserves the modified properties of the TiO_2 nanobuilding blocks, resulting in morphological properties that are advantageous for the photocatalytic H_2 production from methanol (CH_3OH) oxidation. By controlling the amount of Pd doping and Pd nanoparticle loading, the nanoparticle-based aerogels showed significantly improved photoexcited charge generation and separation efficiency under visible light. In addition, we present a novel reactor design specifically developed for 3D aerogel monoliths that allows control of light intensity, gas flow, reactant concentration, and temperature, enabling the study of all key experimental parameters to optimize photocatalytic H_2 production. The visible light absorbed by the aerogels was found to be the driving force behind the efficient photocatalytic activity. Our Pd modified TiO_2 nanoparticle-based aerogels achieved H_2 production rate of 117.5 mmol g^{-1} h^{-1} with good stability for 3 days under visible light thanks to the prevention of carbon monoxide (CO) poisoning. The simultaneous optimization of the material composition and the matching photoreactor form the decisive basis for getting the most out of monolithic 3D photocatalysts.

Received 19th May 2022
Accepted 12th August 2022

DOI: 10.1039/d2ta04024g

rsc.li/materials-a

Introduction

The development of renewable energy sources is of significant importance to meet the ever-increasing energy demands. H_2 as a clean energy carrier holds great potential for a sustainable energy solution, and the concept of H_2 generation based on photocatalyst semiconductors is a promising avenue given the abundance of solar energy as the driving source. The photocatalytic H_2 production relies on a chemical reaction, in which water (H_2O) and/or alcohols (*e.g.*, CH_3OH) react with electrons and holes generated by the photocatalysts under illumination.[1] Compared to H_2O, CH_3OH is a more practical reactant for H_2 production due to its rapid oxidation by photogenerated holes and high proton density.[2] The use of CH_3OH from waste biomass as an H_2 source makes such a process sustainable, and therefore the photocatalytic H_2 production from CH_3OH or a mixture of CH_3OH and H_2O has been extensively studied.[3,4]

Among the many photocatalysts, TiO_2 offers chemical stability, low price, abundance, and a strong oxidation power for H_2O and CH_3OH.[5] The continuous interest in TiO_2 has focused on morphological development from 0D (nanoparticles)[6] to 1D (rods) and 2D (films) nanostructures,[7,8] and finally, 3D architectures like aerogels have appeared with photocatalytically favorable characteristics such as high surface area and open porosity.[9] Macroscopic TiO_2 nanoparticle-based aerogels, built from colloidal nanoparticle dispersions prepared by the nonaqueous sol–gel method, translate the advantageous morphology and the intrinsic properties of the crystalline semiconducting nanoparticles into the final centimeter scaled architecture.[10] The high potential of TiO_2 nanoparticle-based aerogels as efficient 3D photocatalysts in combination with metal co-catalysts (Au and Pd) has been demonstrated for gas-phase reactions such as CO_2 reduction and H_2 production.[11,12] However, TiO_2 nanoparticle-based aerogels work mainly under UV light, which occupies only 4% of

[a]Laboratory for Multifunctional Materials, Department of Materials, ETH Zurich, Vladimir-Prelog-Weg 5, 8093 Zürich, Switzerland

[b]Institute for Chemistry and Bioanalytics, School of Life Sciences, FHNW University of Applied Sciences and Arts Northwestern, Hofackerstrasse 30, 4132 Muttenz, Switzerland. E-mail: markus.niederberger@mat.ethz.ch

† Electronic supplementary information (ESI) available. See https://doi.org/10.1039/d2ta04024g

the solar spectrum due to the large band gap of TiO_2. For TiO_2 aerogels to function efficiently under ordinary sunlight, the band gap of the TiO_2 nanobuilding blocks needs to be modified before or after forming their monolithic bodies.

There are many strategies to make TiO_2 responsive to visible light. One frequently applied method is to dope nonmetals into TiO_2 to narrow the band gap by forming new energy levels above the valence band.[13] Nitrogen doping works particularly well, because it has a similar ionic radius like oxygen and requires less energy for substitution.[14] We have recently demonstrated that Pd modified TiO_2 nanoparticle-based aerogels can easily be doped with nitrogen by a facile gas-phase process, resulting in a photocatalyst that significantly outperformed the undoped material in visible light-driven H_2 production.[15] In addition to nonmetal doping, metal doping into TiO_2 can also improve the optical properties and the photocatalytic activity. Depending on the type of metals, either a new donor (above the valence band) or acceptor (below the conduction band) energy level in the band structure of TiO_2 is generated.[16,17] Moreover, defects such as oxygen vacancies and Ti^{3+} can be introduced due to the difference in the valence states of dopant ions and Ti^{4+}, forming an additional energy level below the conduction band.[18] These altogether contribute to the narrowing of the band gap of TiO_2. Metal-modified TiO_2 aerogels were prepared, for example, from metal-doped TiO_2 nanoparticles as building blocks or by co-gelation of colloidal solutions of metal and TiO_2 nanoparticles. In both cases, the final aerogels suffered from relatively low surface areas of 96.0 and 99 $m^2\ g^{-1}$ and porosities of only 0.36 and 0.33 $cm^3\ g^{-1}$, respectively, due to the high-temperature (500–550 °C) required for crystallizing the amorphous nanoparticles.[19,20] TiO_2 nanoparticle-based aerogels prepared from building blocks that were obtained by the nonaqueous sol–gel route do not need high-temperature annealing, because the as-synthesized anatase nanoparticles are highly crystalline.[21] For efficient photocatalysis, TiO_2 aerogels have to be composed of visible light-absorbing nanobuilding blocks. Microwave-assisted nonaqueous sol–gel routes have emerged as promising methods for metal doping of metal oxides (*e.g.*, TiO_2) because they provide fast, uniform, and direct heating of solvents.[22–24] For example, the method has successfully been adopted to the synthesis of TiO_2 mesocrystals and their doping with Sb and Nb to enhance the photocatalytic degradation of organic dyes.[25] Only a few TiO_2 aerogels followed the microwave approach and delivered a good surface area of 299 $m^2\ g^{-1}$ with an average pore size of 14.5 nm.[26]

Besides doped nanoparticles, it is also possible to use non-doped TiO_2 nanoparticles in combination with noble metal nanoparticles (*e.g.*, Pt, Pd, and Au) for visible light-induced photocatalytic applications.[27–29] Among these metals, Pd functions as particularly effective photocatalyst because of the generation of hot electrons from the $4d^{10}$ orbital under visible-light irradiation.[30] For example, Pd on ZrO_2 creates hot electrons *via* Pd 4d interband transition, which interact with the reactant molecules on the Pd surface, inducing effective dehydrogenation of benzyl alcohol at a wavelengths below 620 nm.[31] In addition, Pd-TiO_x photofield-effect transistors revealed the highest photocurrent at 450 nm in the visible spectrum, indicating that the injection of the highest-energy electrons from Pd into TiO_2 occurs at this wavelength.[32] For such electron transfer, it is essential that the photoinduced electrons in Pd have enough energy to overcome the Schottky barrier formed at the interface between Pd and TiO_2 and transfer to the conduction band of TiO_2.

For the production of large amounts of H_2 with Pd modified TiO_2 photocatalysts under visible light, the Pd nanoparticles need to be well distributed on the surface of TiO_2. Moreover, the amount of energetic electrons that are excited under visible light and injected into TiO_2 or reacted with educt molecules has to be high. TiO_2 as the photocatalyst and support should have a large surface area and high porosity, as it is ideally provided by the morphology of aerogels. Although Pd-containing TiO_2 aerogels have been studied their performance under visible light was considerably lower than at UV light due to the lack of the appropriate optical properties.[12] In addition to the photoabsorption properties and the ability to generate and separate charge carriers during the photocatalysis under visible-light illumination, it is important to regulate the type and quantity of the various products formed during the photocatalytic process. For example, during H_2 production by CH_3OH oxidation, CO as one of the potential by-products affects the activity of Pd by poisoning its active sites on the surface and, consequently, impacts the performance and stability of the photocatalyst.[33,34]

This study reports a fast and effective one-pot synthesis of Pd modified TiO_2 nanoparticles using a microwave reactor and the subsequent processing of the nanobuilding blocks into macroscopic aerogels as 3D photocatalysts. Only 15 min is enough to produce the crystalline Pd modified TiO_2 nanoparticles. Our approach enables the doping of TiO_2 with Pd ions and the simultaneous distribution of Pd nanoparticles on TiO_2. This gives us the unique opportunity to both improve optical properties of TiO_2 and prepare the required co-catalyst in only one step, which greatly facilitates the synthesis of visible light-active photocatalysts. Accordingly, the Pd modified TiO_2 aerogels were investigated for the photocatalytic H_2 production from CH_3OH oxidation using a custom-made gas-phase photoreactor that can be heated. This makes it possible to investigate the temperature influence on the photocatalytic performance of aerogels in addition to the effects of Pd doping and Pd nanoparticle loading. We have recently shown that for macroscopic 3D photocatalysts, reactor design plays an important role in addition to material composition.[35] Together with light intensity and gas flow, we are now able to systematically optimize all important experimental parameters for maximum H_2 production.

Experimental

Materials

Titanium(IV) tetrachloride ($TiCl_4$, 99.9% trace metals basis), benzyl alcohol (BnOH, puriss., 99–100.5% (GC)), 2-amino-2-(hydroxymethyl)-1,3-propanediol (Trizma® base, puriss., ≥99.7%), palladium(II) acetate ($[Pd(OAc)_2]_3$, ≥99.9% trace metals basis) and methanol (MeOH, analytical grade) were

purchased from Sigma-Aldrich. Acetone (99.8%, extra dry) was purchased from Acros Organics, and ethanol (absolute, >99.8% for analysis), chloroform (≥99.8%) and diethyl ether (≥99.5%) were purchased from VWR Chemicals. Liquid carbon dioxide (≥99%), argon (Ar, 99.999%), helium (He, 99 999%) and nitrogen (N_2, 99.999%) were provided by PanGas AG, Switzerland. All chemicals were used as received without further purification.

Microwave synthesis of TiO_2 nanoparticle dispersion

$TiCl_4$ (1 mL) and Trizma (92 mg) were added into 20 mL of BnOH and stirred until dissolved.[36] The solution was transferred to a microwave tube (35 mL) sealed with a teflon cap and heated in a microwave reactor (CEM Discover, 2.45 GHz) for 15 min at 80 °C. The synthesized TiO_2 nanoparticles were washed three times with chloroform and diethyl ether, and 10 mL of deionized water was added to the wet nanoparticles. After centrifugation of this mixture, the aqueous phase with the TiO_2 nanoparticles was collected by a syringe. The residual diethyl ether in the dispersion was removed by applying a vacuum. The concentration of the TiO_2 dispersion in deionized water was 70 mg mL^{-1}.

One-step synthesis of Pd modified TiO_2 nanoparticle dispersion

$[Pd(OAc)_2]_3$ (36, 48, 60 or 72 mg) was added in to a mixture of $TiCl_4$ (1 mL) and Trizma (92 mg) in BnOH (20 mL). The mixture was microwave treated for 15 min at 80 °C. The steps for washing, adding water, collection of the Pd modified TiO_2 dispersion, and removing the residual diethyl ether were the same as for the TiO_2 nanoparticle dispersion. The Pd modified TiO_2 concentrations of the aqueous dispersions using 36, 48, 60, and 72 mg of $[Pd(OAc)_2]_3$ were 63, 72, 78, and 84 mg mL^{-1}, respectively.

Step-wise synthesis of Pd loaded TiO_2 nanoparticle dispersion

TiO_2 nanoparticles were prepared with the same microwave process as above, and the resulting suspension was centrifuged. Pd nanoparticles were prepared separately by reacting $[Pd(OAc)_2]_3$ (48 mg) in BnOH (20 mL) for 15 min at 80 °C in the microwave reactor. The synthesized Pd nanoparticles in BnOH were combined with the TiO_2 precipitate. The mixed solution was washed with chloroform and diethyl ether three times. Finally, the wet precipitate containing both types of nanoparticles was dispersed in 10 mL of water. The Pd loaded TiO_2 dispersion was collected by a syringe. The residual diethyl ether in the dispersion was also removed by applying a vacuum. The concentration of the Pd loaded TiO_2 dispersion in water was 71 mg mL^{-1}.

Aerogel fabrication

0.3 mL of the different nanoparticle dispersions were mixed with 0.3 mL of ethanol. Gelling was carried out in an oven at 60 °C for 27 min. The gelation step is quantitative, *i.e.*, all the nanoparticles in the dispersion are incorporated in the gel. The samples were then solvent-exchanged by immersing them into solvent mixtures with different volume ratios in the following order: acetone/ethanol/water = 70/20/10 (v/v%) for 20 h, 80/15/5 (v/v%) for 6 h and 100/0/0 (v/v%) for 20 h. The gels were supercritically dried in a SPI-DRY Critical Point Dryer 13 200, replacing the acetone with supercritical CO_2. The aerogels were treated with UV light (2000 W) using a Hönle UVACUBE 2000 chamber for 10 h and flipped over and treated again for 10 h to remove organic residues on the surface. The supercritically dried aerogels were annealed in air at 150 °C for 1 h using a furnace (Carbolite EHA Compact). Out of 10 aerogels prepared, about 8 have the required quality to be used in the photocatalytic tests, while the rest cracks and falls apart during the solvent exchange. The aerogels prepared with the different amounts of $[Pd(OAc)_2]_3$ (36, 48, 60, and 72 mg) were labeled as Pd1–TiO_2, Pd2–TiO_2, Pd3–TiO_2, and Pd4–TiO_2, respectively. The theorical atomic percentage (at%) of Pd in Pd loaded TiO_2, Pd1–TiO_2, Pd2–TiO_2, Pd3–TiO_2, and Pd4–TiO_2 is calculated as 2.25, 2.25, 2.85, 3.39, and 3.85, respectively. The Pd content in the respective aerogels as obtained by X-ray photoelectron spectroscopy (XPS) is 0.21, 0.29, 0.59, 0.65, and 0.75 at%. The typical weight of an aerogel monolith is 18 mg.

Characterization

X-ray diffraction (XRD) patterns of the powdered aerogels were measured by a PANalytical Empyrean with a PIXcel 1D detector and Cu Kα radiation. Raman spectroscopy was performed on aerogels using NT-MPT Spectrum Instruments with a laser wavelength of 473 nm. High-resolution transmission electron microscopy (HRTEM) and scanning transmission electron microscopy (STEM) images were taken with a FEI Talos F200X microscope operated at 200 kV. Ultra-high resolution scanning electron microscope (SEM) (Hitachi SU8200) was operated at 1 kV. Nitrogen gas sorption of aerogels was performed on a Quantachrome Autosorb iQ analyzer at 77 K. The surface area was determined by Brunauer–Emmett–Teller (BET) method, and the pore size and pore volume were measured by density functional theory (DFT) analysis using a Non-Local DFT (NLDFT) calculation model for nitrogen at 77 K based on cylindrical pores in silica. JASCO V-770 spectrophotometer equipped with an ILN-725 integrating sphere was used to measure the UV-Vis diffuse reflectance spectra of the powdered aerogels. X-ray photoelectron spectroscopy (XPS) was conducted by a Sigma 2 spectrometer (Thermo Scientific) using a polychromatic Al Kα X-ray source by taking C1s = 284.8 eV as the calibration peak. The atomic concentration was calculated from the individual peak area of Ti, O, and Pd and their respective atomic sensitivity factor. Electrochemical measurements were conducted with Biologic VMP3 in a three-electrode cell configuration with Ag/AgCl as the reference electrode and a platinum wire as the counter electrode. The powdered aerogel (10 mg) was dispersed in ethanol (1 mL) and coated on FTO glass as the working electrode. Aqueous Na_2SO_4 solution (0.5 M) was used as the electrolyte, and a white LED (Thorlabs, wavelength range of 400–800 nm) irradiated the system during measurement. Nyquist plots were recorded by electrochemical impedance

spectroscopy (EIS) in the frequency range of 0.1–100 kHz with an ac amplitude of 5 mV under an open circuit.

Photocatalytic H_2 production test

Gas-phase photocatalytic H_2 production was conducted under visible-light irradiation. The aerogel was placed in a custom-built electrically heated gas flow reactor, which we call Q-master. The complete Q-master reactor system is composed of a gas preparation system, a reactor chamber, and a gas analysis system (Fig. S1†). The reactor system has two white LEDs (Thorlabs, wavelength range of 400–800 nm), which are used with a collimation adapter. They are attached to both sides of the reactor chamber (Fig. S2†). The system has thermal insulators made of teflon installed between the LEDs and the reactor chamber to minimize thermal effects. Detailed information on the individual components of the reactor system can be found in Fig. S3.† Pd1–TiO_2, Pd2–TiO_2, Pd3–TiO_2, Pd4–TiO_2, TiO_2, and Pd loaded TiO_2 aerogels were measured at 40 °C. In the gas preparation system, Ar as a carrier gas was bubbled through a mixture of CH_3OH and H_2O (50 : 50 v/v%) with a flow rate of 20 mL min^{-1}, and the vapors were delivered to the aerogel. TiO_2 and Pd2–TiO_2 aerogels were additionally measured at 60, 80, and 100 °C. At 100 °C, the Pd modified TiO_2 aerogel was additionally investigated at different flow rates of 20, 30, and 40 mL min^{-1} and under different CH_3OH to H_2O ratios (50 : 50, 80 : 20, and 100 : 0 v/v%). Moreover, different LED wavelengths (385, 430, 450, and 660 nm) were tested on Pd2–TiO_2 at 100 °C with 80 : 20 v/v% of CH_3OH and H_2O. In the analysis system, a gas chromatograph (INFICON Micro-GC 3000A, equipped with He and Ar carrier gas) monitored the H_2 production with a thermal conductivity detector, and the H_2 rate was evaluated by the amount obtained after 2 h. The apparent quantum efficiency was determined as reported before.[15]

Results and discussion

Pd modified TiO_2 nanoparticles were synthesized using a straightforward one-step microwave-assisted nonaqueous sol–gel route, in which $TiCl_4$ and $[Pd(OAc)_2]_3$ were reacted simultaneously with benzyl alcohol in the presence of Trizma. After washing the synthesized Pd modified TiO_2 nanoparticles with nonpolar solvents, we added H_2O to prepare the dispersion, which is stable for 6 months (Fig. S4†). The dispersion was destabilized to form a gel, which was subsequently supercritically dried. The prepared aerogels were UV-treated and annealed in air. The aerogels had a pellet-like shape, and thickness of the pellet of 2.5 mm was chosen under consideration of the light penetration depth of 1.7–2.7 mm as found before.[37,38] A digital photograph of the monolithic Pd modified TiO_2 aerogels (Pd1–TiO_2, Pd2–TiO_2, Pd3–TiO_2, and Pd4–TiO_2) is displayed in Fig. 1a. With increasing amount of Pd precursor, the color of the aerogels becomes darker, implying that more Pd is incorporated in the aerogels, improving visible-light absorption. XRD characterization was performed to investigate the crystal structures of the powdered TiO_2, Pd1–TiO_2, Pd2–TiO_2, Pd3–TiO_2, and Pd4–TiO_2 aerogels (Fig. 1b). All the patterns show that TiO_2 is present in the anatase phase (ICDD 01-070-6826). The samples with Pd, except the Pd1–TiO_2, additionally contain a peak at 38.9°, corresponding to Pd (111). All samples show high crystallinity even before annealing at 150 °C (Fig. S5a†), suggesting that our microwave-assisted nonaqueous sol–gel method offers crystalline TiO_2 nanobuilding blocks with Pd nanocrystals at low temperature. Compared to the other anatase reflections, the (004) peak is sharper due to the oriented attachment of Trizma-functionalized TiO_2 nanoparticles along [001] as previously observed.[36] Note that the Pd peak (111) increases with increasing Pd concentration. In Pd1–TiO_2 the Pd peak is not visible due to the small amount of Pd. To study the effect of Pd addition on the crystal growth of the titania nanoparticles, the (101) reflection of anatase in the XRD patterns of TiO_2, Pd1–TiO_2, Pd2–TiO_2, Pd3–TiO_2, and Pd4–TiO_2 are plotted in Fig. S5b.† The Pd modification results in peak broadening and slight shift of the peak position to smaller 2θ values relative to TiO_2, which can be attributed to the substitution of Ti^{4+} (0.61 Å) by the larger Pd^{2+} (0.64 Å) in the anatase lattice.[39,40] The crystal sizes of Pd1–TiO_2, Pd2–TiO_2, Pd3–TiO_2, and Pd4–TiO_2 calculated by the Scherrer equation considering the (101) (200) and (105) reflections are 6.1, 5.8, 5.8, and 6.2 nm, respectively, which are smaller than that (6.9 nm) of TiO_2 (Table S1†). The structural changes of Pd modified TiO_2 aerogels with different amounts of Pd were additionally monitored by Raman spectroscopy (Fig. 1c). The Raman spectra of TiO_2, Pd1–TiO_2, Pd2–TiO_2, Pd3–TiO_2, and Pd4–TiO_2 show six Raman active modes ($3E_g$, $2B_{1g}$, and A_{1g}) that are typical for the anatase phase of TiO_2,[41] confirming the results obtained from XRD data. The two peaks (A_{1g} and B_{1g}) located around 520 cm^{-1} overlap, thus resulting in one broad peak. Note that the strongest band (E_g) in the Pd modified TiO_2 samples shows a noticeable shift and broadening compared to TiO_2, whereas the Pd loaded TiO_2 sample exhibits a similar spectrum like TiO_2 (Fig. S6a and b†). The band shift and broadening can be attributed to internal strain induced by introducing Pd^{2+} into the TiO_2 crystal.[42] Incorporation of Pd^{2+} into the lattice of anatase and formation of Pd–O bonds leads to the distortion and change of bond distances of Ti–O bonds compared to pure TiO_2.[40] As a result, the vibration energy of the E_g peak corresponding to the Ti–O bond bending vibration changes.

Scanning transmission electron microscopy (STEM) and high-resolution transmission electron microscopy (HRTEM) analyses were carried out to check the morphology, the structure, and the composition of the Pd modified TiO_2 (Pd2–TiO_2) nanoparticles. The STEM image in Fig. 2a presents individual Pd nanoparticles on the surface of interconnected TiO_2 nanoparticles in Pd2–TiO_2 nanoparticle-based aerogel. Fig. 2b shows a HRTEM image of a Pd nanoparticle with an approximate size of 10 nm size and well-developed lattice fringes with a spacing of 0.22 nm, corresponding to the (111) plane. The particles are attached on the interconnected TiO_2 nanoparticles, which are oriented along the [001] direction, confirming the XRD results.[43] The crystal size of the Pd nanoparticles ranges from 6 nm to 24 nm with an average value of 12.4 nm (Fig. S7a–d†). A scanning electron microscopy (SEM) image of the Pd2–TiO_2 aerogel in Fig. 2c reveals a continuous network of nanoparticles with

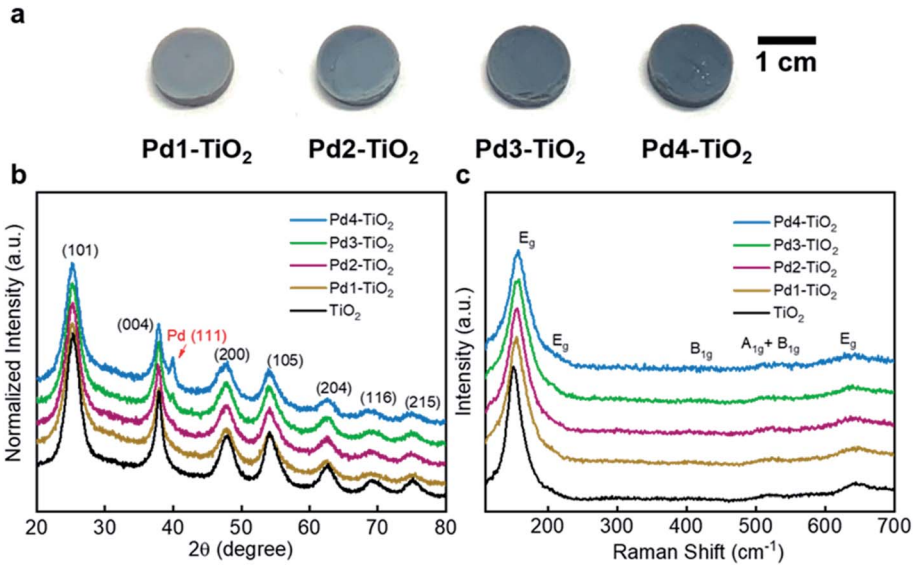

Fig. 1 (a) Digital photograph of Pd1–TiO_2, Pd2–TiO_2, Pd3–TiO_2, and Pd4–TiO_2 aerogel monoliths. (b) XRD patterns and (c) Raman spectra of powdered TiO_2, Pd1–TiO_2, Pd2–TiO_2, Pd3–TiO_2, and Pd4–TiO_2 aerogels.

open pores. Energy-dispersive X-ray spectroscopy (EDXS) analyses in high-angle annular dark-field (HAADF) imaging mode were carried out to investigate the elemental spatial distribution in Pd2–TiO_2 (Fig. S8a†). The EDXS maps of Ti, Pd, and O were obtained from the same area of the aerogel, and the signals of the elements were detected over the whole aerogel area (Fig. S8b–d†). The concentrated Pd signals in the EDXS map of Pd are from the Pd nanoparticles on the surface of TiO_2 aerogel. The Pd detected over the whole volume in the map presumably results from Pd doping in TiO_2.

N_2 gas sorption analysis was performed to investigate the morphological properties such as surface area and porosity of TiO_2, Pd1–TiO_2, Pd2–TiO_2, Pd3–TiO_2, and Pd4–TiO_2 aerogels. The adsorption–desorption isotherms are of type IV with hysteresis loops characteristic for mesoporous materials (Fig. 2d). This observation is consistent with the pore size distribution analysis by density functional theory (DFT), which confirms the existence of mesopores (Fig. 2e). The aerogels composed of Pd1–TiO_2, Pd2–TiO_2, Pd3–TiO_2, and Pd4–TiO_2 nanoparticles offer a surface area of 422.7, 420.7, 416.5, and 387.0 $m^2\ g^{-1}$ and pore volume of 1.422, 1.395, 1.352, and 1.265 $cm^3\ g^{-1}$ (Table S1†). Accordingly, the surface area and pore volume decreases with increasing amount of Pd, and this trend also includes pure TiO_2 with a surface area of 433.2 $m^2\ g^{-1}$ and a pore volume of 1.892 $cm^3\ g^{-1}$. The reduction in the surface area and pore volume was the most pronounced for Pd4–TiO_2, probably due to the largest amount of the Pd nanoparticles interrupting the oriented attachment of TiO_2 nanoparticles during the gelation process. In spite of this negative effect of Pd, the surface areas and pore volumes are still very high, underlining that the one-pot microwave-assisted benzyl alcohol route is conducive for producing Pd-doped TiO_2 nanoparticles along with Pd nanoparticles as building blocks for aerogels in just one step.

The chemical composition and in particular the Pd concentration of Pd1–TiO_2, Pd2–TiO_2, Pd3–TiO_2, and Pd4–TiO_2 aerogels were evaluated by X-ray photoelectron spectroscopy (XPS). First, Pd 3d spectra were deconvoluted into the three regions, as shown in Fig. 3a. The peak located at the lowest binding energy (335.3 eV) can be assigned to metallic Pd nanoparticles loaded on the surface of TiO_2 aerogel.[44] The second peak at 336.5 eV is attributed to oxidized Pd (PdO), which formed during the UV treatment and annealing of the aerogels in air.[45] The last peak positioned at 337.6 eV agrees well with XPS data of Pd^{2+} incorporated into the TiO_2 crystal lattice.[40,46] The reason for having two separate peaks for Pd^{2+} as dopant and PdO nanoparticles on the surface of TiO_2 is that the chemical environment of Pd^{2+} in TiO_2 is quite different to the one of Pd^{2+} in PdO. The amount of Pd doping *vs.* formation of Pd and PdO nanoparticles was analyzed and plotted in Fig. 3b. A higher amount of Pd precursor during the synthesis leads to a higher amount of Pd and PdO nanoparticles loaded on the surface, which agrees well with the XRD results. The concentration of Pd and PdO nanoparticles increases from 0.25% (Pd1–TiO_2) to 0.50% (Pd2–TiO_2), 0.57% (Pd3–TiO_2), and 0.66% (Pd4–TiO_2). For Pd doping, adding the highest amount of Pd precursor during the synthesis does not result in higher Pd doping. Pd1–TiO_2 exhibits a lower doping level (0.04%) compared to the other three samples (Pd2–TiO_2, Pd3–TiO_2, and Pd4–TiO_2), which show the same amount of dopant concentration (0.09%, 0.08%, and 0.09%). The results indicate that although our method makes it possible to continuously increase the Pd concentration in the sample in the form of metallic Pd and PdO nanoparticles as a function of the precursor concentration, the doping itself is limited. Pd loaded TiO_2 aerogel contained 0.21% Pd and PdO nanoparticles (Fig. S9a†). Due to the different valence states of Ti^{4+} and $Pd^{2+}$and the resulting excess of electrons we expect the presence

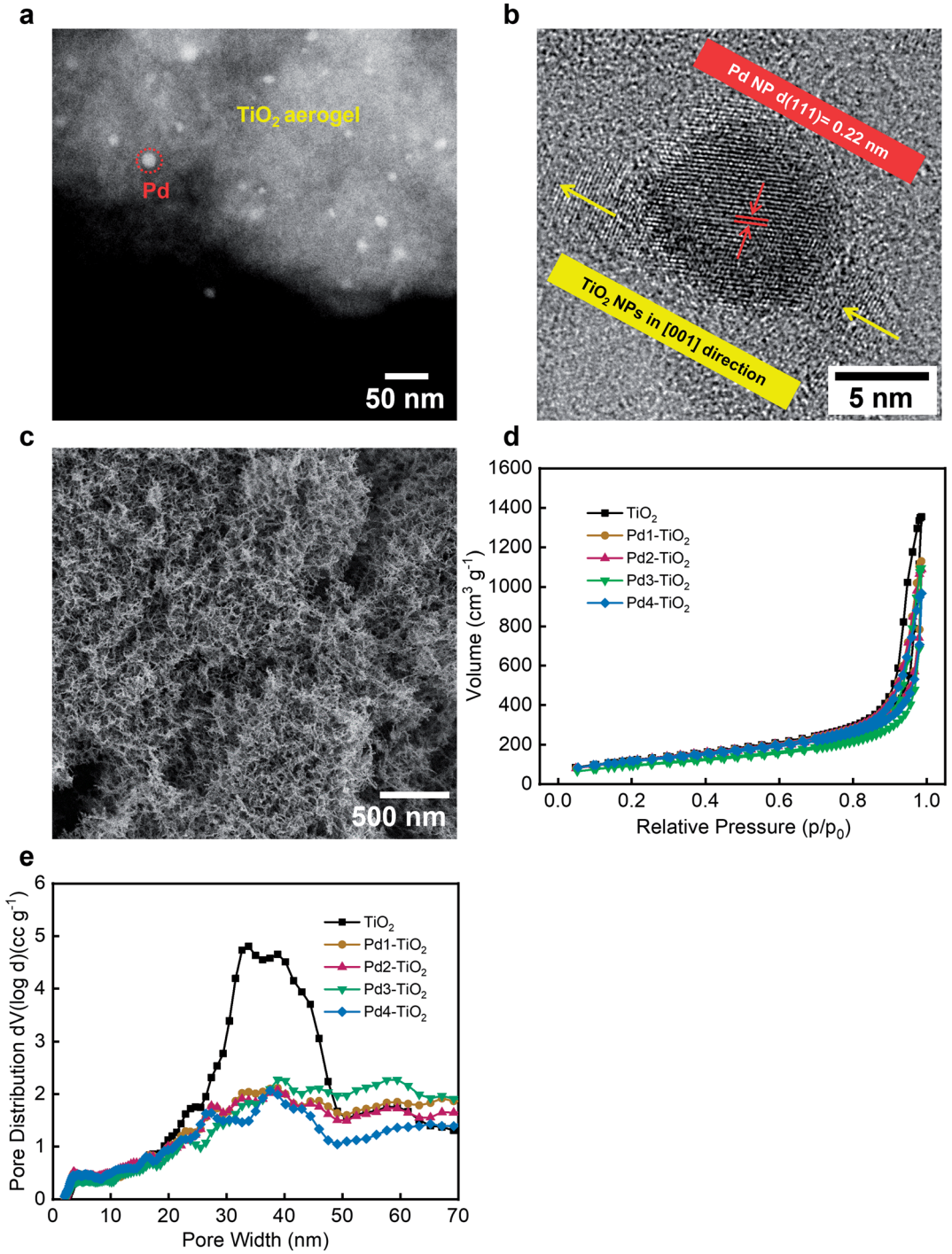

Fig. 2 (a) STEM image and (b) HRTEM image of a powdered Pd2–TiO_2 aerogel. (c) SEM image of a fraction of Pd2–TiO_2 aerogel. (d) N_2 adsorption–desorption isotherms and (e) DFT pore size distribution of TiO_2, Pd1–TiO_2, Pd2–TiO_2, Pd3–TiO_2, and Pd4–TiO_2 aerogels.

of Ti^{3+}.[40] XPS Ti 2p analysis indeed supports that Pd1–TiO_2, Pd2–TiO_2, Pd3–TiO_2, and Pd4–TiO_2 aerogels have Ti^{3+} as defects. Compared to the TiO_2 aerogel, Ti 2p peaks in Pd1–TiO_2, Pd2–TiO_2, Pd3–TiO_2, and Pd4–TiO_2 aerogels are shifted to lower binding energy because of the more reduced state of Ti ions (Fig. S10a†). The atomic percentage of Ti^{3+} in the Pd modified TiO_2 samples increases from 4.9 to 6.0% and stays at 6.3 and 6.3%, respectively, following the same trend like the Pd dopant concentration (Fig. S10b–e†). The valence band edge was studied by XPS to elucidate the electronic structure of TiO_2 and Pd modified TiO_2 (Fig. 3c). Compared to TiO_2 and Pd loaded TiO_2 that have the same onset of the valence band edge (Fig. S9b†), the Pd modified TiO_2 aerogels show an obvious shift of the onset of the valence band edge with a wide hump. This observation indicates that new energy states formed above the valence band due to the Pd ions doped into the TiO_2

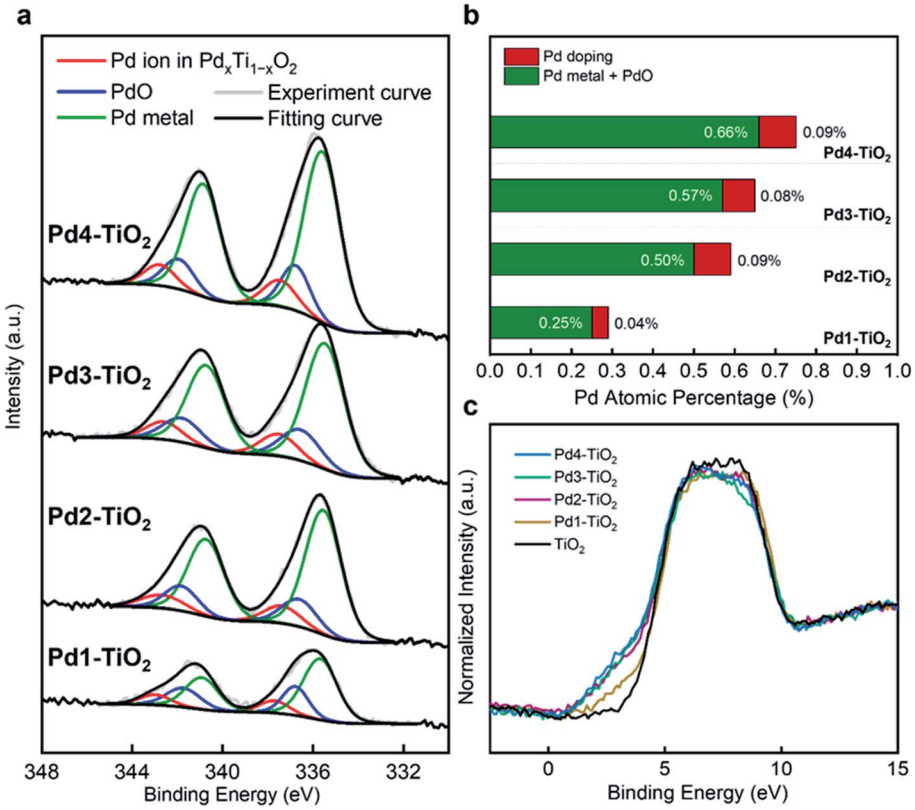

Fig. 3 (a) XPS Pd 3d spectra and (b) atomic percentage of Pd doping and Pd nanoparticle loading of Pd1–TiO_2, Pd2–TiO_2, Pd3–TiO_2, and Pd4–TiO_2 aerogels. (c) XPS valence band spectra of TiO_2, Pd1–TiO_2, Pd2–TiO_2, Pd3–TiO_2, and Pd4–TiO_2 aerogels.

nanostructure.[47,48] In addition, a higher Pd dopant concentration leads to a higher density of energy states, accordingly, generating a narrower band gap. However, the valence band edges in Pd2–TiO_2, Pd3–TiO_2, and Pd4–TiO_2 remain almost identical, which is well-aligned with the same doping level of the samples. The XPS valence band of TiO_2 modified by Pd doping is one of the indications for enhanced visible-light absorption.

The optical properties were studied to investigate the effect of the Pd doping and Pd nanoparticle loading on TiO_2, and therefore, UV-visible absorption spectra of powdered TiO_2, Pd1–TiO_2, Pd2–TiO_2, Pd3–TiO_2, and Pd4–TiO_2 aerogels were measured (Fig. 4a). As electrons transfer from the 2p valence band of O to the 3d conduction band of Ti, the TiO_2 aerogel shows only absorbance below 400 nm in the UV region.[5] Note that in Pd1–TiO_2, Pd2–TiO_2, Pd3–TiO_2, and Pd4–TiO_2 the absorption edge is shifted to the visible region with substantial absorption over a broad range of wavelengths from 400–800 nm. Such a band edge shift implies that Pd doping modifies the band gap of TiO_2, improving the visible-light sensitivity. It can be inferred that the enhanced absorption of these samples in the visible region is a result of the excitation of the new energy level formed by 4d electrons of Pd ions above the valence band to the conduction band.[49,50] The presence of oxygen vacancies and Ti^{3+} as observed by XPS analysis form the energy levels below the conduction band.[51] Accordingly, these new energy levels in the band gap of TiO_2 help to enhance the visible-light absorption of Pd1–TiO_2, Pd2–TiO_2, Pd3–TiO_2, and Pd4–TiO_2 aerogels. In addition, the optical properties are further improved by the Pd nanoparticles on the surface.[31,32] The spectra show the trend that with increasing amount of Pd nanoparticles on the TiO_2 aerogels a higher visible-light response is obtained. Pd4–TiO_2, which according to XRD and XPS possesses the highest amount of Pd on the surface, absorbs visible light the most compared to the other samples. The absorption in the range of 400–550 nm can be attributed to the d–d transitions of the partially oxidized Pd nanoparticles.[52] The Pd loaded TiO_2 aerogel also display visible-light absorption, but no shift in the absorption edge (Fig. S11a†). Even with an amount of Pd nanoparticles comparable to Pd1–TiO_2 in a similar size range, as confirmed by XPS and TEM (Fig. S9a and S11b†), the response to visible light was much lower for Pd loaded TiO_2. All these results imply that a number of factors including Pd doping, oxygen vacancies, Ti^{3+}, and partially oxidized Pd nanoparticles contribute to the efficient visible-light sensitivity of Pd1–TiO_2, Pd2–TiO_2, Pd3–TiO_2, and Pd4–TiO_2 aerogels. Such enhanced optical properties of the samples are promising for photocatalysis.

The average photocatalytic H_2 production rate with standard deviation of three identical aerogels of TiO_2, Pd1–TiO_2, Pd2–TiO_2, Pd3–TiO_2, and Pd4–TiO_2 was measured from CH_3OH oxidation under visible light (Fig. 4b). Photocatalytic reactions using macroscopic aerogel monoliths have to be performed in the gas phase, because the contact with liquid reactants causes

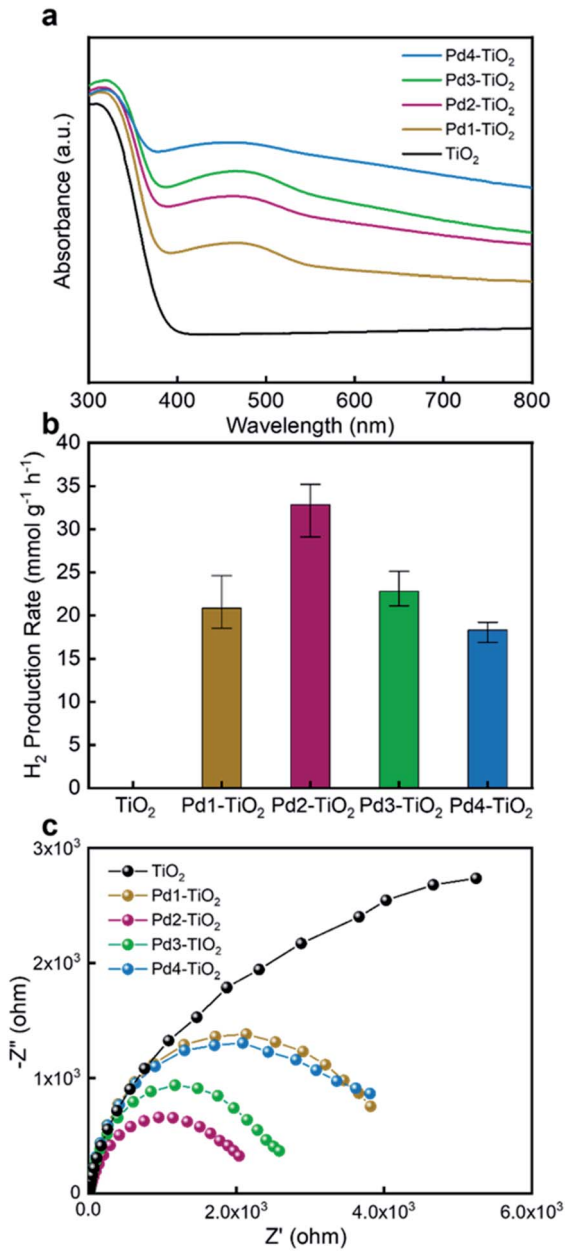

Fig. 4 (a) UV-visible absorption spectra, (b) visible light-driven photocatalytic H_2 production rates and (c) EIS Nyquist plots of TiO_2, Pd1–TiO_2, Pd2–TiO_2, Pd3–TiO_2, and Pd4–TiO_2 aerogels.

pulverization of the aerogels due to strong capillary forces. The monolithic aerogel was directly loaded in a custom-built continuous gas flow reactor (Q-master), which can be heated (Fig. S1†). The reactor was designed in such a way that the aerogel can be placed perpendicular to the two Thorlabs White LEDs (wavelength range of 400–800 nm) to maximize illumination of the aerogel (Fig. S3†). The LEDs were installed with a collimation adaptor to achieve a more uniform intensity of light on the aerogel. The temperature of the reactor chamber increased to 40 °C after turning on the LEDs. Our aerogel was fabricated in the shape of a 2.5 mm thick pellet, as a previous study showed that light penetrates about 1.7–2.7 mm into the monolith.[37,68] Ar as a carrier gas (20 mL min^{-1}) was bubbled through a mixture of CH_3OH and H_2O (50 : 50 v/v%) and guided into the reactor chamber. A gas chromatograph measured the H_2 amount. As shown in Fig. 4b, the TiO_2 aerogel showed no H_2 production, because it does not absorb visible light. In contrast, Pd1–TiO_2, Pd2–TiO_2, Pd3–TiO_2, and Pd4–TiO_2 aerogels produced significant amounts of H_2, and the highest rate of 32.8 mmol g^{-1} h^{-1} was observed for Pd2–TiO_2. The increase in H_2 production of Pd modified TiO_2 compared to that of TiO_2 results from the improvement of the optical properties by Pd doping and Pd nanoparticle loading, which enable the generation of electrons and holes under visible light. The H_2 production rate of 13.7 mmol g^{-1} h^{-1} in Pd loaded TiO_2 aerogel proves that hot electrons can be generated *via* the 4d interband transition in Pd nanoparticles under visible light (Fig. S11c†).[31,53,54] In addition to this positive contribution of the Pd nanoparticles to the photoactivity in the visible region, electrons from the energy level above the valence band created by the Pd doping can be excited into the conduction band, further promoting the photocatalytic activity in the visible region.[55] The presence of oxygen vacancies and Ti^{3+} also helps the performance by forming localized states below the conduction band. They act as electron acceptors for better charge separation and respond to visible light.[56,57] Compared to Pd2–TiO_2, the Pd1–TiO_2 aerogel produced only 20.8 mmol g^{-1} h^{-1}, which was due to the lower visible-light absorption resulting from the low Pd doping and Pd nanoparticle loading in the TiO_2 aerogel. At the same time, the Pd1–TiO_2 aerogel shows a higher H_2 production rate than Pd loaded TiO_2, although both aerogels have a similar amount of Pd nanoparticle loading, suggesting that the Pd modified TiO_2 aerogels prepared by the one-pot synthesis are more efficient visible light-active photocatalysts (Fig. S11c†). On the other hand, despite high sensitivity to visible light, Pd3–TiO_2 and Pd4–TiO_2 showed lower rates of 22.8 and 18.3 mmol g^{-1} h^{-1}, respectively, implying that an excess of Pd nanoparticles on the surface can be detrimental for H_2 production. This is because the Pd nanoparticles on the outer surface of the aerogel monolith inhibit light from penetrating into the center of the monolith.[58] To confirm the hypothesis of the shading effect on the photocatalytic activity, only one LED was installed to illuminate the aerogel (Fig. S12†). The H_2 production rates of Pd3–TiO_2 and Pd4–TiO_2 achieved only 35.8% and 30.05% of the rates obtained with two LEDs, whereas 40.8% and 40.7% were produced by Pd1–TiO_2 and Pd2–TiO_2, respectively. The differences in H_2 production rates reflects the variation in light penetration depth, because the light interferes more strongly with the samples with high Pd nanoparticle loadings. In addition, an increase in the Schottky barrier between Pd and TiO_2 induced by a larger amount of Pd can make the electron transfer from Pd to Pd-doped TiO_2 or *vice versa* difficult, deteriorating the activity.[29] In addition to the shadowing effect, it has been reported that large concentrations of Pd nanoparticles can act as charge recombination centers, which may further contribute to the reduction in activity.[59,60] These results suggest that there is an optimum Pd doping and Pd nanoparticle loading of the TiO_2 aerogels to promote visible-light absorption and facilitate charge generation and transfer efficiently. Pd2–TiO_2, obviously,

has the ideal composition for an efficient H_2 production. A direct comparison of our results with literature data is difficult due to rather different photocatalytic measurement conditions such as reactor type, light source, and sacrificial agent. However, considering materials with the same composition (Pd modified TiO_2), visible-light illumination, low reaction temperature, and use of CH_3OH and H_2O, our H_2 production rate is among the best reported to date.[61–63]

Electrochemical impedance spectroscopy (EIS) measurements were performed to evaluate the transfer efficiency of the photoinduced charge carriers of TiO_2, Pd1–TiO_2, Pd2–TiO_2, Pd3–TiO_2, and Pd4–TiO_2 aerogels. All the Nyquist plots were obtained under visible-light illumination (Fig. 4c). TiO_2 shows the largest semicircle due to the fast recombination of electrons and holes. In contrast, Pd2–TiO_2 has the smallest semicircle among the samples, indicating that the highest amount of electrons was transferred from Pd-doped TiO_2 to Pd nanoparticles or the other way around due to the optimum amount of Pd doping and Pd nanoparticle loading. Pd3–TiO_2 and Pd4–TiO_2, which have similar Pd doping but a higher amount of Pd nanoparticle loading than Pd2–TiO_2, exhibit semicircles with larger diameters. This observation can be explained by the high Schottky barrier between TiO_2 and Pd induced by the excessive loading of Pd nanoparticles, reducing the charge transfer efficiency, thus increasing the resistance. Pd1–TiO_2 shows a lower conductivity than Pd2–TiO_2 due to the lack of visible-light sensitivity. The EIS results align well with the performance trends of photocatalytic H_2 production and confirm that Pd2–TiO_2 has the optimal Pd doping and Pd nanoparticle loading for TiO_2 aerogels to most efficiently generate and separate photoexcited electrons under visible light.

In the following, we studied the influence of temperature, light intensity, gas flow, and reactant concentrations on the photocatalytic H_2 production rates of Pd2–TiO_2 aerogels. Our custom-made heated gas flow photocatalytic reactor (Q-master) was designed to enable control of all these experimental parameters to investigate the optimal reaction conditions in the macroscopic aerogels. Compared to a reactor where the photocatalysis takes place in liquid phase, we are not limited by the boiling point of the CH_3OH and H_2O mixture. In this study we investigated the photocatalytic H_2 production at 40, 60, 80, and 100 °C using TiO_2 and Pd2-TiO_2 aerogels under visible-light irradiation (Fig. 5a). As the temperature of the reactor was increased stepwise from 40 to 100 °C, the average H_2 production rate of Pd2–TiO_2 was also increased from 32.8 to 51.7, 74.6, and finally, it reached 85.4 mmol g^{-1} h^{-1} at 100 °C. According to the literature, applying temperature can promote the kinetic energy of the reactant molecules.[64] Furthermore, a temperature increase leads to an enhanced gas diffusion rate, or, in other words, the lower resistance of the gas transport can accelerate the photocatalytic reaction.[65] This behavior was also observed in our aerogels, which generated more H_2 with increasing temperatures with the highest average H_2 production rate at 100 °C. Stability is another important factor in the evaluation of a photocatalyst and thus long-term measurements were carried out. As shown in Fig. 5b, the Pd2–TiO_2 aerogel demonstrates stable H_2 generation for 72 h with average rates of 39.2, 55.4, 79.8, and 86.9 mmol g^{-1} h^{-1} at 40, 60, 80, and 100 °C, respectively. However, looking at the trend of the stability of H_2 production, we find that Pd2–TiO_2 accelerated the H_2 rate the most at 100 °C at the beginning, but then dropped faster than at lower temperatures, reaching a similar amount as at 80 °C at the end. Moreover, the final product CO also slowly decreased, and compared to 80 °C a higher amount of the intermediate formaldehyde (CH_2O) started to be detected after 18 h (Fig. S13a and b†). The results indicate that the ability of oxidizing CH_3OH in Pd2–TiO_2 to produce H_2 degraded over time at 100 °C, which was also observed at 80 °C after extending the measurement to 100 h (Fig. S13c†). But even for 100 h, the average production rate of 85.3 mmol g^{-1} h^{-1} was still very high. The decline in H_2 production with time is probably due to the surface of Pd being poisoned by a high amount of CO formed during CH_3OH oxidation, causing the gradual deactivation of Pd2–TiO_2 as photocatalyst. Literature data indeed indicate that the CO molecules, as reaction products or intermediates, block the active sites of the metal surface, inhibiting the reaction.[33]

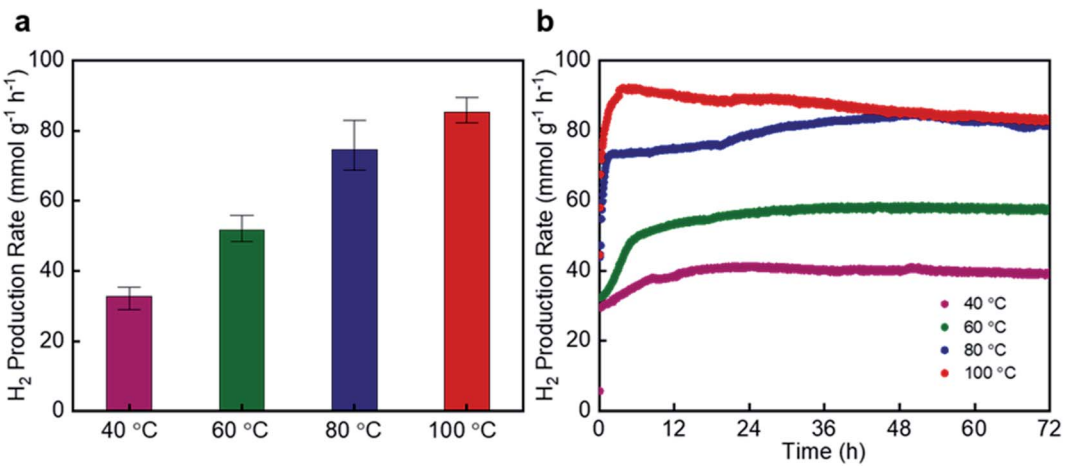

Fig. 5 (a) Visible light-driven photocatalytic H_2 production rates and (b) stability test of Pd2–TiO_2 aerogels at different reactor temperatures (40, 60, 80, and 100 °C).

Therefore, it is crucial to simultaneously keep the CO amount low and the H_2 production rate high, which will be discussed later, to achieve stable and high performance of photocatalytic H_2 production.

To identify the role of light for H_2 generation, we evaluated Pd2–TiO_2 without illumination under a continuous flow of the reactant vapors. As shown in Fig. S14a,† no H_2 was detected at 40, 60, 80, and 100 °C, emphasizing that the generation of H_2 is only driven by photoexcited charge carriers supported by heat energy. We also investigated the reaction at the temperature of 120 °C. Small amounts of H_2 were detected, indicating that the effect of thermal catalyst begins at this temperature. No H_2 was detected for the TiO_2 aerogel without Pd modification with illumination even at 100 °C. The observation that TiO_2 aerogels cannot produce H_2 even under high temperatures implies that the enhanced optical property is essential for producing photogenerated charge carriers under visible light. When the light intensity was controlled by changing the LED current (0.2, 0.35, 0.5, and 0.7 A) using T-Cube™ LED Driver, the H_2 production rates increased with the light intensity independent of the temperature (Fig. S14b†). These results prove that the visible light absorbed by Pd2–TiO_2 is the driving force for photocatalytic reactions.

The gas flow determines how much H_2 can be produced per time unit and therefore it is important to optimize it. Different gas flow rates (20, 30, and 40 mL min^{-1}) were tested on Pd2–TiO_2 at 100 °C. As shown in Fig. S14c,† a flow rate of 30 and 40 mL min^{-1} leads to 79.1 and 78.7 mmol g^{-1} h^{-1} of H_2, which is less efficient than 88.3 mmol g^{-1} h^{-1} at 20 mL min^{-1}. It seems that the complete oxidation of CH_3OH is compromised at faster flow rates of 30 and 40 mL min^{-1}. Obviously, under these conditions the reaction does not have enough time to proceed completely on the aerogel. This is reflected by the noticeable increase of the intermediate CH_2O with increasing flow rates (Fig. S14c†).[66] Based on these results, 20 mL min^{-1} corresponds to the ideal gas flow rate for photocatalytic H_2 production *via* CH_3OH oxidation with Pd2–TiO_2.

Given the fact that CO poisoning causes a drop in H_2 production compromising the long-term stability, we explored different concentration ratios of CH_3OH and H_2O (50 : 50, 80 : 20, and 100 : 0 v/v%) to find conditions that can reduce the poisoning effect of CO while producing a high H_2 production rate. As displayed in Fig. 6a, our Pd2–TiO_2 aerogel appears to rapidly accelerate the H_2 production at 100 v/v% CH_3OH, reaching a maximum of 118.1 mmol g^{-1} h^{-1} after 5 h, but then dropping by 26.4% after 72 h. A noticeable decline in the H_2 production rate is due to the high amount of CO generated, which can poison the active sites at the surface of the Pd nanoparticles, lowering their catalytic activity over time (Fig. 6b). In comparison, the stability was much better for 50 : 50 and 80 : 20 v/v%, with H_2 production rates of 92.2 and 120.2 mmol g^{-1} h^{-1} in the first 5 h, which decreased by 10.2%

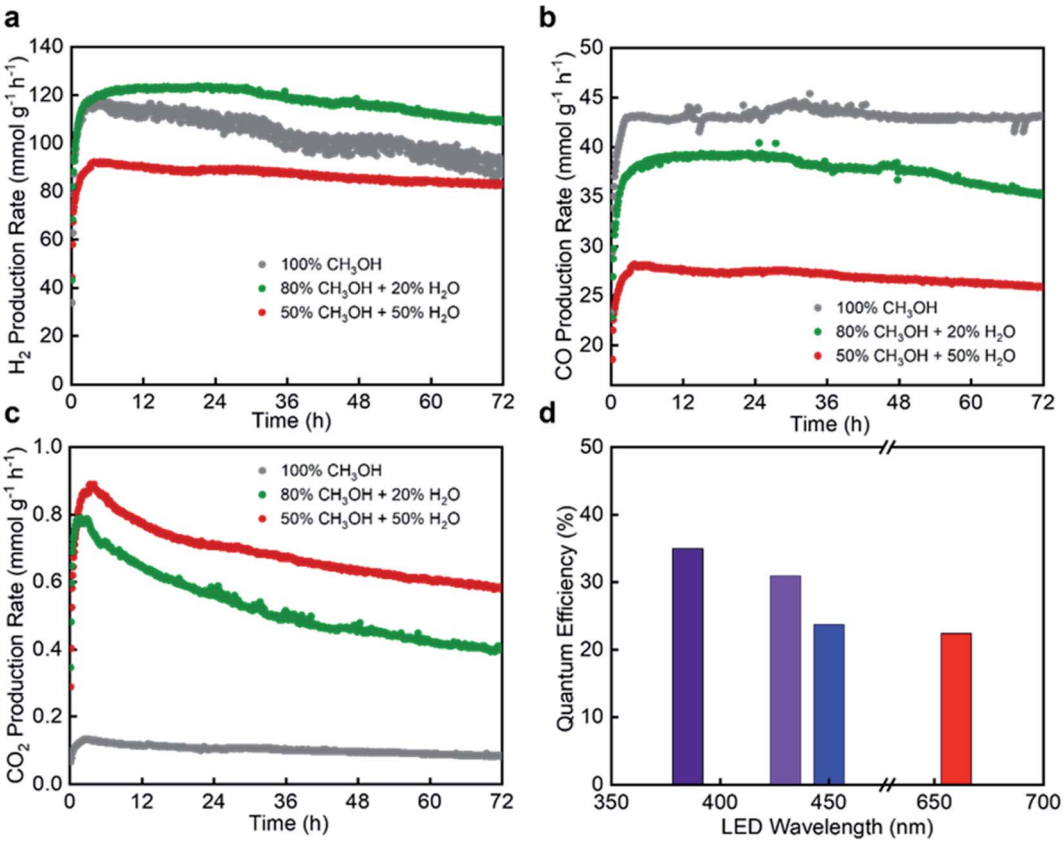

Fig. 6 Results for visible light-driven CH_3OH oxidation using Pd2–TiO_2 aerogels at 100 °C with different CH_3OH-to-H_2O ratios: (a) H_2 production rates, (b) CO production rates and (c) CO_2 production rates. (d) QE of Pd2–TiO_2 aerogels at 100 °C under different wavelengths of LEDs.

and 8.9% after 72 h, respectively. Moreover, the two samples formed less CO while generating more CO_2 compared to the reaction with 100 v/v% CH_3OH, which may be caused by the oxidation reaction of CO to CO_2 by H_2O (Fig. 6c). Indeed, literature indicates that H_2O has a positive effect on CO oxidation by lowering the activation energy or introducing OH groups for CO oxidation.[67,68] Thus, our study demonstrates that the presence of H_2O in CH_3OH oxidation is beneficial to suppress CO poisoning of aerogels, and thus maintain the efficiency of the photocatalytic reaction at a high level over a long period of time. The synergetic effect between the morphology of the aerogels (highly porous and large surface area), the enhanced optical properties (Pd modification of the TiO_2 nanoparticles), and the carefully controlled reaction conditions (temperature, light intensity, gas flow rate, and CH_3OH-to-H_2O ratio) allows us to achieve a high H_2 production rate of 117.5 mmol g^{-1} h^{-1} over 72 h. Considering that the complete consumption of 1 mole of CH_3OH in the presence of H_2O generates 3 moles of H_2, our aerogel shows a conversion efficiency of 24.4% in this reaction.

The apparent quantum efficiency (QE) was measured under the same conditions as the photocatalytic tests. The reactor was irradiated by LEDs with different wavelengths (385, 430, 450, and 660 nm) under optimized conditions (gas flow rate: 20 mL min^{-1}, temperature: 100 °C) and concentration of the reactants (CH_3OH-to-H_2O ratio: 80 : 20 v/v%). As shown in Fig. 6d, the Pd2–TiO_2 aerogel achieved the highest QE of 35% under UV. Under this condition, a large number of photogenerated charge carriers are produced in TiO_2 and Pd-doped TiO_2, which can be transferred to the Pd nanoparticles as the electron sink. However, even in the visible region of 430 and 450 nm, the QE of 30.9 and 23.7% obtained with Pd2–TiO_2 are comparable with UV data, suggesting that Pd and Pd-doped TiO_2 can also generate a significant amount of charge carriers under visible light. Note that 22.4% QE was achieved at 660 nm in Pd2–TiO_2, while Pd loaded TiO_2 aerogel did not offer as high QE as it did below 450 nm, which is similar to the other reported papers (Fig. S15†).[31,32] The results indicate that the extended activation range of Pd2–TiO_2 up to 660 nm originates largely from Pd doping. The Pd doping and the resulting oxygen vacancies and Ti^{3+} in TiO_2 contribute to a narrower band gap, which in turn enables the generation of photoexcited carriers at a longer wavelength. Our one-pot synthesis method for Pd modified TiO_2 nanoparticles using microwave-assisted nonaqueous sol–gel method produces two different types of Pd species, namely Pd ions incorporated in the TiO_2 lattice and metallic Pd nanoparticles loaded on the surface of the TiO_2 nanoparticles. These Pd modified TiO_2 nanoparticles are perfect building blocks for high-quality macroscopic aerogels with high surface areas of 421 m^2 g^{-1} and large pore volumes of 1.395 cm^3 g^{-1}. HRTEM and STEM analyses indicate well dispersed crystalline Pd nanoparticles on the TiO_2 aerogel matrix. XRD, Raman, and XPS analyses confirm that the aerogel network is composed of Pd-doped TiO_2 nanoparticles, providing a narrow band gap as the result of the formation of Pd 4d energy levels above the valence band and additional energy levels from the presence of oxygen vacancies and Ti^{3+} in TiO_2. As we increase the initial concentration of the Pd precursor, the Pd doping and the resulting defect concentration also increase until it reaches a saturation level. If the Pd precursor concentration is increased beyond this point, only the Pd nanoparticle loading increases, indicating that we can control the amount of Pd nanoparticle loading while keeping the Pd doping constant. Although Pd doping and Pd nanoparticle loading increase the visible-light absorption, an excess of Pd nanoparticles on the surface of the aerogel can adversely affect charge generation and separation due to the shadowing effect and the high Schottky barrier. The photocatalytic H_2 production rate combined with photoelectrochemical measurements allow us

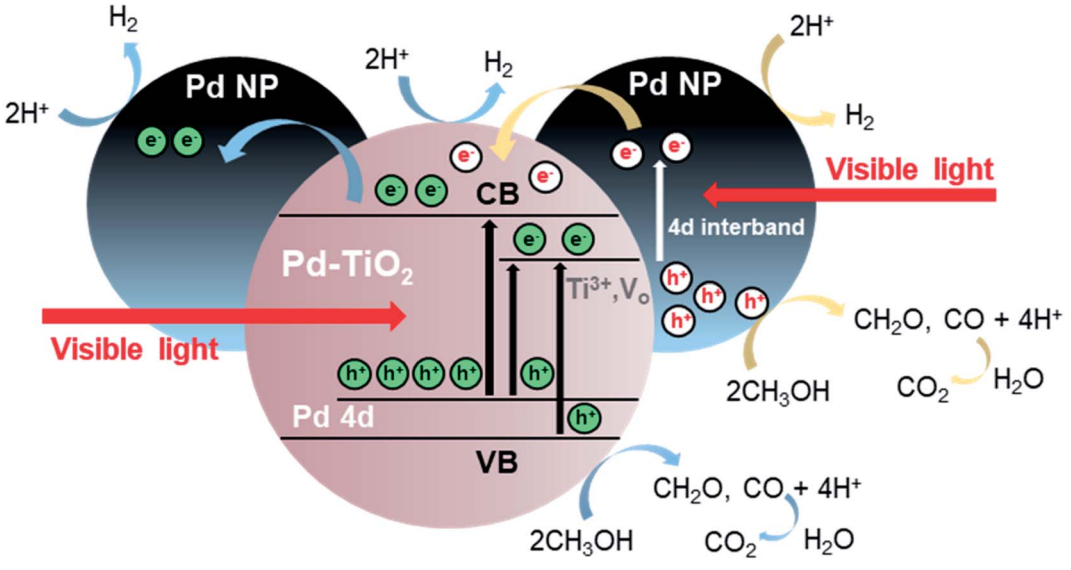

Fig. 7 Schematic illustration of the different chemical and physical processes occurring during the photocatalytic H_2 production from CH_3OH oxidation in Pd modified TiO_2 aerogels.

to assess the best performing Pd modified TiO_2 aerogels with the optimal amount of Pd doping and Pd nanoparticle loading to achieve a H_2 production rate of 31.6 mmol g^{-1} h^{-1} at 40 °C. In addition to the composition of the photocatalyst, the careful study and optimization of experimental parameters related to the gas-phase reaction in the reactor, such as temperature, light intensity, and gas flow rate, is another way to increase H_2 production. As a final parameter, the concentration ratio of CH_3OH and H_2O was optimized, which not only resulted in the highest H_2 generation rate of 117.5 mmol g^{-1} h^{-1}, but also improved the long-term stability by preventing the degradation of photocatalytic ability due to CO poisoning.

Based on our investigations, we propose a mechanism for the photocatalytic H_2 production by CH_3OH oxidation under visible light (Fig. 7). The energy level of Pd 4d states above the valence band of TiO_2 enables the absorption of visible light, creating charge carriers in Pd-doped TiO_2. Energy levels introduced by the defects help the charge generation and separation. In parallel, also the Pd nanoparticles on the surface respond to visible light, producing hot electrons and holes by the 4d interband transition. As a consequence, the photogenerated holes oxidize CH_3OH into CH_2O and CO, offering $4H^+$ (eqn (S1)). The photoinduced electrons in Pd-doped TiO_2 can transfer to the adjacent Pd nanoparticle, where they reduce $2H^+$ to H_2. The hot electrons excited in the Pd nanoparticles either migrate to TiO_2 or they stay on the surface of Pd, where they react with $2H^+$ to produce H_2. In the presence of H_2O, another oxidation process can take place, namely the conversion of CO to CO_2, which lowers the deactivation of the photocatalytic activity of the Pd modified TiO_2 aerogel.

Conclusions

A fast and simple nonaqueous one-pot sol–gel route using a microwave reactor gives access to Pd modified TiO_2 nanoparticles as highly crystalline and visible light-responsive building blocks for macroscopic nanoparticle-based aerogels. The Pd modified TiO_2 nanoparticles preserve their intrinsic properties in the 3-dimensional monolithic body, giving the aerogel a large surface area and high porosity. A unique feature of the synthesis is that it leads to both Pd doping and Pd nanoparticle loading of TiO_2 in one step, both of which contribute significantly to the photocatalytic activity of the aerogels. The combination of two different states of Pd in TiO_2 is ideal to promote the generation and separation of photoexcited charge carriers to enhance the photocatalytic CH_3OH oxidation for efficient H_2 production under visible light. Through the development of a flexible reactor design, we have been able to carefully study the effects of reactor temperature, light intensity, and gas flow rate to systematically optimize the reaction conditions in terms of H_2 production rate. By adjusting the reactant concentrations, the poisoning of the surface of the Pd nanoparticles by CO can be reduced, which in turn increases the performance and also the long-term stability of the Pd modified TiO_2 nanoparticle-based aerogel photocatalysts. Our best sample in the heated gas flow reactor was able to produce 117.5 mmol g^{-1} h^{-1} of H_2 over a period of 3 days under visible-light illumination. Our results show that in addition to optimizing the composition of the photocatalytically active material, the reactor design must also be tailored to fully exploit the potential of 3-dimensional photocatalysts for visible-light reactions.

Conflicts of interest

There are no conflicts to declare.

Acknowledgements

Financial support by ETH Zürich is gratefully acknowledged. We especially thank Till Kyburz for designing, producing, and discussion for the Q-master reactor.

Notes and references

1 J. Corredor, M. J. Rivero, C. M. Rangel, F. Gloaguen and I. Ortiz, *J. Chem. Technol. Biotechnol.*, 2019, **94**, 3049–3063.
2 W.-C. Lin, W.-D. Yang, I. L. Huang, T.-S. Wu and Z.-J. Chung, *Energy Fuels*, 2009, **23**, 2192–2196.
3 J. Zhao, R. Shi, Z. Li, C. Zhou and T. Zhang, *Nano Sel.*, 2020, **1**, 12–29.
4 P. Gautam, Neha, S. N. Upadhyay and S. K. Dubey, *Fuel*, 2020, **273**, 117783.
5 J. Schneider, M. Matsuoka, M. Takeuchi, J. Zhang, Y. Horiuchi, M. Anpo and D. W. Bahnemann, *Chem. Rev.*, 2014, **114**, 9919–9986.
6 X.-J. Zheng, L.-F. Wei, Z.-H. Zhang, Q.-J. Jiang, Y.-J. Wei, B. Xie and M.-B. Wei, *Int. J. Hydrogen Energy*, 2009, **34**, 9033–9041.
7 W. Chen, Y. Wang, S. Liu, L. Gao, L. Mao, Z. Fan, W. Shangguan and Z. Jiang, *Appl. Surf. Sci.*, 2018, **445**, 527–534.
8 R. Dholam, N. Patel, M. Adami and A. Miotello, *Int. J. Hydrogen Energy*, 2008, **33**, 6896–6903.
9 M. Niederberger, *Adv. Funct. Mater.*, 2017, **27**, 1703647.
10 F. Rechberger and M. Niederberger, *Nanoscale Horiz.*, 2017, **2**, 6–30.
11 F. Rechberger and M. Niederberger, *Mater. Horiz.*, 2017, **4**, 1115–1121.
12 A. L. Luna, F. Matter, M. Schreck, J. Wohlwend, E. Tervoort, C. Colbeau-Justin and M. Niederberger, *Appl. Catal., B*, 2020, **267**, 118660.
13 H. Liu and L. Gao, *J. Am. Ceram. Soc.*, 2004, **87**, 1582–1584.
14 R. Asahi, *Science*, 2001, **293**, 269–271.
15 J. Kwon, K. Choi, M. Schreck, T. Liu, E. Tervoort and M. Niederberger, *ACS Appl. Mater. Interfaces*, 2021, **13**, 53691–53701.
16 S. George, S. Pokhrel, Z. Ji, B. L. Henderson, T. Xia, L. Li, J. I. Zink, A. E. Nel and L. Mädler, *J. Am. Chem. Soc.*, 2011, **133**, 11270–11278.
17 V. Kumaravel, S. Mathew, J. Bartlett and S. C. Pillai, *Appl. Catal., B*, 2019, **244**, 1021–1064.
18 C. Di Valentin, G. Pacchioni and A. Selloni, *J. Phys. Chem. C*, 2009, **113**, 20543–20552.

19 H. S. Kibombo, A. S. Weber, C.-M. Wu, K. R. Raghupathi and R. T. Koodali, *J. Photochem. Photobiol., A*, 2013, **269**, 49–58.
20 J. Puskelova, L. Baia, A. Vulpoi, M. Baia, M. Antoniadou, V. Dracopoulos, E. Stathatos, K. Gabor, Z. Pap, V. Danciu and P. Lianos, *Chem. Eng. J.*, 2014, **242**, 96–101.
21 F. J. Heiligtag, M. D. Rossell, M. J. Süess and M. Niederberger, *J. Mater. Chem.*, 2011, **21**, 16893–16899.
22 I. Bilecka and M. Niederberger, *Electrochim. Acta*, 2010, **55**, 7717–7725.
23 D. Primc, M. Bärtsch, D. Barreca, G. Carraro, C. Maccato, C. Sada and M. Niederberger, *Sustainable Energy Fuels*, 2017, **1**, 199–206.
24 I. Bilecka, L. Luo, I. Djerdj, M. D. Rossell, M. Jagodič, Z. Jagličić, Y. Masubuchi, S. Kikkawa and M. Niederberger, *J. Phys. Chem. C*, 2011, **115**, 1484–1495.
25 D. Primc, G. Zeng, R. Leute, M. Walter, L. Mayrhofer and M. Niederberger, *Chem. Mater.*, 2016, **28**, 4223–4230.
26 S. Alwin, X. S. Shajan, K. Karuppasamy and K. G. K. Warrier, *Mater. Chem. Phys.*, 2017, **196**, 37–44.
27 W. Zhai, S. Xue, A. Zhu, Y. Luo and Y. Tian, *ChemCatChem*, 2011, **3**, 127–130.
28 A. Kumar, P. Choudhary, A. Kumar, P. H. C. Camargo and V. Krishnan, *Small*, 2022, **18**, 2101638.
29 Y. Shiraishi, D. Tsukamoto, Y. Sugano, A. Shiro, S. Ichikawa, S. Tanaka and T. Hirai, *ACS Catal.*, 2012, **2**, 1984–1992.
30 Z. Li and X. Meng, *J. Alloys Compd.*, 2020, **830**, 154669.
31 S. Sarina, H.-Y. Zhu, Q. Xiao, E. Jaatinen, J. Jia, Y. Huang, Z. Zheng and H. Wu, *Angew. Chem., Int. Ed.*, 2014, **53**, 2935–2940.
32 L. Chen, S. Mao, P. Wang, Z. Yao, Z. Du, Z. Zhu, L. A. Belfiore and J. Tang, *Adv. Opt. Mater.*, 2021, **9**, 2001505.
33 Y. Zhou, D. E. Doronkin, Z. Zhao, P. N. Plessow, J. Jelic, B. Detlefs, T. Pruessmann, F. Studt and J.-D. Grunwaldt, *ACS Catal.*, 2018, **8**, 11398–11406.
34 M. Bowker, C. Morton, J. Kennedy, H. Bahruji, J. Greves, W. Jones, P. R. Davies, C. Brookes, P. P. Wells and N. Dimitratos, *J. Catal.*, 2014, **310**, 10–15.
35 F. Matter and M. Niederberger, *Adv. Sci.*, 2022, **9**, 2105363.
36 J. Polleux, N. Pinna, M. Antonietti, C. Hess, U. Wild, R. Schlögl and M. Niederberger, *Chem. Eur. J.*, 2005, **11**, 3541–3551.
37 M. Schreck, N. Kleger, F. Matter, J. Kwon, E. Tervoort, K. Masania, A. R. Studart and M. Niederberger, *Small*, 2021, **17**, 2104089.
38 A. L. Luna, S. Papadopoulos, T. Kyburz, E. Tervoort, L. Novotny and M. Niederberger, *J. Mater. Chem. A*, 2021, **9**, 22380–22391.
39 R. D. Shannon, *Acta Crystallogr.*, 1976, **32**, 751–767.
40 B. D. Mukri, G. Dutta, U. V. Waghmare and M. S. Hegde, *Chem. Mater.*, 2012, **24**, 4491–4502.
41 U. Balachandran and N. G. Eror, *J. Solid State Chem.*, 1982, **42**, 276–282.
42 A. N. Banerjee, N. Hamnabard and S. W. Joo, *Ceram. Int.*, 2016, **42**, 12010–12026.
43 J. Polleux, N. Pinna, M. Antonietti and M. Niederberger, *Adv. Mater.*, 2004, **16**, 436–439.
44 M. C. Militello and S. J. Simko, *Surf. Sci. Spectra*, 1994, **3**, 387–394.
45 E. H. Voogt, A. J. M. Mens, O. L. J. Gijzeman and J. W. Geus, *Surf. Sci.*, 1996, **350**, 21–31.
46 S. Roy, A. Marimuthu, M. S. Hegde and G. Madras, *Appl. Catal., B*, 2007, **73**, 300–310.
47 A. Gupta, M. S. Hegde, K. R. Priolkar, U. V. Waghmare, P. R. Sarode and S. Emura, *Chem. Mater.*, 2009, **21**, 5836–5847.
48 S. Roy, M. S. Hegde, N. Ravishankar and G. Madras, *J. Phys. Chem. C*, 2007, **111**, 8153–8160.
49 P. Bera and M. S. Hegde, *RSC Adv.*, 2015, **5**, 94949–94979.
50 F. Dong, P. Li, J. Zhong, X. Liu, Y. Zhang, W. Cen and H. Huang, *Appl. Catal., A*, 2016, **510**, 161–170.
51 B. Bharti, S. Kumar, H.-N. Lee and R. Kumar, *Sci. Rep.*, 2016, **6**, 32355.
52 Z. Zhang, G. Mestl, H. Knözinger and W. M. H. Sachtler, *Appl. Catal., A*, 1992, **89**, 155–168.
53 C. Xu, W. Huang, Z. Li, B. Deng, Y. Zhang, M. Ni and K. Cen, *ACS Catal.*, 2018, **8**, 6582–6593.
54 X. Z. Ji and G. A. Somorjai, *J. Phys. Chem. B*, 2005, **109**, 22530–22535.
55 L. Chang, G. Zhu, Q.-U. Hassan, B. Cao, S. Li, Y. Jia, J. Gao, F. Zhang and Q. Wang, *Langmuir*, 2019, **35**, 11265–11274.
56 F. Amano, M. Nakata, A. Yamamoto and T. Tanaka, *J. Phys. Chem. C*, 2016, **120**, 6467–6474.
57 T. K. Rahul, M. Mohan and N. Sandhyarani, *ACS Sustainable Chem. Eng.*, 2018, **6**, 3049–3059.
58 K. C. Christoforidis and P. Fornasiero, *ChemCatChem*, 2017, **9**, 1523–1544.
59 J. Xu, X. Liu, Z. Zhou, L. Deng, L. Liu and M. Xu, *Energy Fuels*, 2021, **35**, 10820–10831.
60 C. Wang, L. Yin, L. Zhang, N. Liu, N. Lun and Y. Qi, *ACS Appl. Mater. Interfaces*, 2010, **2**, 3373–3377.
61 U. Caudillo-Flores, M. J. Muñoz-Batista, J. A. Cortés, M. Fernández-García and A. Kubacka, *Mol. Catal.*, 2017, **437**, 1–10.
62 U. Caudillo-Flores, M. J. Muñoz-Batista, M. Fernández-García and A. Kubacka, *Appl. Catal., B*, 2018, **238**, 533–545.
63 X. Li, P. Wang, B. Huang, X. Qin, X. Zhang, Q. Zhang, X. Zhu and Y. Dai, *Int. J. Hydrogen Energy*, 2017, **42**, 25195–25202.
64 B. Han and Y. H. Hu, *J. Phys. Chem. C*, 2015, **119**, 18927–18934.
65 S. Guo, X. Li, J. Li and B. Wei, *Nat. Commun.*, 2021, **12**, 1343.
66 M. Schreck and M. Niederberger, *Chem. Mater.*, 2019, **31**, 597–618.
67 A. Manasilp and E. Gulari, *Appl. Catal., B*, 2002, **37**, 17–25.
68 F. Liang, H. Zhu, Z. Qin, H. Wang, G. Wang and J. Wang, *Catal. Lett.*, 2008, **126**, 353–360.